The Journal of Green Energy and Environmental Engineering

Research Paper

Colorimetric Detection of Ascorbic Acid and Total Antioxidant Capacity Based on CoNi Bimetallic Metal Organic Framework

Arjun Kapoor[1,*], Tahir Quraishi[2]

[1] Department of Chemical Engineering, Khalifa University of Science and Technology, P.O. Box 127788, Abu Dhabi, United Arab Emirates
[2] Institute of Chemistry, Federal University of Rio Grande do Sul (UFRGS), Porto Alegre, RS, Brazil
*Corresponding author: kapoor@itbhu.ac.in; tquraishi@gmail.com

Abstract. A bimetallic CoNi metal–organic framework (CoNi-MOF) was fabricated through a room-temperature co-precipitation approach. Leveraging the synergistic interplay between cobalt and nickel, the bimetallic framework demonstrated markedly enhanced oxidase-mimicking activity relative to its single-metal counterparts, enabling it to catalyse the oxidation of the chromogenic probe 3,3',5,5'-tetramethylbenzidine (TMB) and generate a distinct colour response. This chromogenic process was strongly suppressed upon introduction of ascorbic acid (AA). Accordingly, a colourimetric assay for AA quantification was developed. The sensing system displayed a linear response to AA spanning 1–16 µmol/L, with a detection limit of 0.34 µmol/L (S/N = 3), alongside excellent specificity and prolonged shelf-life. Its practical utility was validated through the determination of total antioxidant capacity (TAC) in fresh fruit specimens and commercially available beverages. Recovery tests on spiked passion fruit samples yielded values between 98.17 % and 101.30 %, with relative standard deviations (RSDs) remaining under 7 %. Without addition of H_2O_2, this detection system was simple to operate and low in cost, which provided a new analytical method for food quality monitoring and antioxidant capacity evaluation, and expanded new horizons for application of bimetallic MOF nanozymes in sensing analysis.

Keywords: *Metal organic frameworks; Oxidase like activity; Colorimetric detection; Ascorbic acid; Total antioxidant capacity*

Received on 02 March 2026, Accepted on 05 June 2026, Published on 07 July 2026

1 Introduction

Ascorbic acid (AA), as an important endogenous antioxidant small molecule in organisms, is not only an essential nutrient for maintaining normal physiological functions, but also a key evaluation index for characterizing food freshness and nutritional value [1-3]. Total antioxidant capacity (TAC) is a core indicator for measuring the comprehensive antioxidant effect of all antioxidant substances in a sample. It can objectively reflect the nutritional health value of food and the overall redox state of the body, and has an indispensable guiding role in dietary nutrition assessment, food processing quality monitoring, and disease prevention research [4-6]. AA and TAC can provide a key basis for the synergistic evaluation of food nutritional value and biological health status. Therefore, establishing a rapid and accurate simultaneous detection method for AA and TAC has important practical significance.

Conventional assays for ascorbic acid and total antioxidant capacity predominantly rely on high-performance liquid chromatography [7], electrochemical techniques [8], and fluorimetric analysis [9]. Such approaches are typically encumbered by laborious protocols, stringent instrumental requirements, protracted turnaround times, and susceptibility to matrix effects, rendering them ill-suited for high-throughput, rapid screening. In contrast, colorimetric sensing has garnered escalating interest in recent years by virtue of its operational simplicity, visually interpretable readout, and minimal equipment demands. Within this domain, nanozyme-driven colorimetric platforms have emerged as a particularly vibrant research frontier [10–11]. The underlying sensing paradigm exploits the enzyme-mimetic catalytic activity of nanomaterials to generate reactive oxygen species

that oxidise a chromogenic reporter; antioxidant analytes then attenuate this chromogenic response by scavenging the ROS, and the magnitude of signal suppression is correlated with antioxidant concentration or capacity [12–13]. Nanozyme colorimetric detection systems are mainly divided into two categories: peroxidase-like (POD) and oxidase-like (OXD). Among them, the POD-like system requires additional addition of hydrogen peroxide (H_2O_2), which easily causes detection deviation due to fluctuations in H_2O_2 concentration; the OXD-like system can directly utilize O_2 in the environmental medium to generate ROS without additional addition of H_2O_2, avoiding detection deviation caused by fluctuations in the concentration of external reagents, and is more suitable for antioxidant capacity analysis of complex matrix samples [14-15].

Within the expanding nanozyme landscape, metal–organic framework (MOF)-derived nanozymes constitute a promising and rapidly evolving material platform. As porous crystalline networks formed through the coordination of metal ions or clusters with organic ligands, MOFs offer remarkably high specific surface areas, tunable pore architectures and electronic properties, alongside abundant, homogeneously distributed metallic active sites [16–17]. Their metal centers can serve as catalytic active sites, and the porous structure is conducive to substrate adsorption and mass transfer, showing excellent enzyme-like catalytic performance. However, single-metal MOFs are limited by the electron transfer efficiency of a single metal center, and their catalytic activity and stability need to be improved [18]. Researchers have proposed a bimetallic MOF modification strategy, which introduces suitable metal ions and utilizes the synergistic effect between metals to regulate the electronic structure, increase defect sites and active sites, and accelerate interfacial electron transfer, thereby significantly enhancing enzyme-like catalytic performance [19-20].

Co and Ni have similar atomic radii and complementary electronic configurations. The bimetallic system formed by them can effectively improve the catalytic performance of redox reactions through synergistic effects such as charge transfer and electron cloud rearrangement [21]. Based on this, this study synthesized a CoNi bimetallic metal-organic framework material (CoNi-MOF) by a room-temperature co-precipitation method. Compared with monometallic MOFs, due to the bimetallic synergistic effect, CoNi-MOF exhibited stronger OXD-like activity. Based on its excellent OXD-like activity, CoNi-MOF can catalyze O_2 to generate ROS, further oxidizing 3,3′,5,5′-tetramethylbenzidine (TMB) to generate a blue product (ox-TMB). When ascorbic acid is introduced, it scavenges the reactive oxygen species generated in the assay, thereby suppressing the chromogenic oxidation of TMB. This attenuation registers as a decline in absorbance at 652 nm, establishing a direct quantitative link between AA concentration and the magnitude of signal loss. Capitalising on this response, a colourimetric detection platform was developed for AA determination and subsequently extended to the evaluation of total antioxidant capacity in fresh produce and commercially available beverages (Fig. 1). The work not only furnishes a practical route for rapid food-quality screening but also opens new analytical vistas for bimetallic MOF nanozymes.

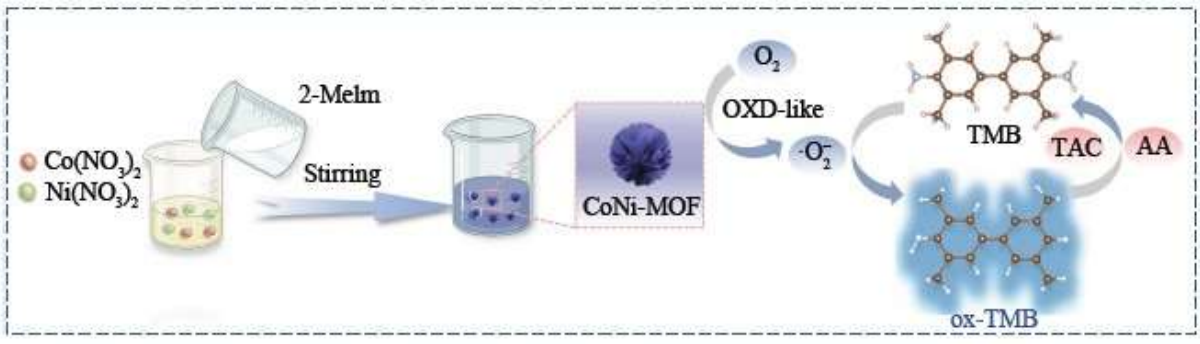

Figure 1 Schematic illustration of the synthesis of cobalt-nickel bimetallic metal-organic framework (CoNi-MOF) and the colorimetric detection mechanism. 2-Melm: 2-methylimidazole; AA: ascorbic acid; TAC: total antioxidant capacity; TMB: 3,3′,5,5′-tetramethylbenzidine; ox-TMB: oxidized TMB; MOF: metal-organic framework; OXD: oxidase

2 Experimental Section

2.1 Instruments and reagents

Morphological and elemental characterisation was performed on a Zeiss Sigma 300 field-emission scanning electron microscope equipped with an energy-dispersive X-ray detector (Zeiss, Germany). Crystalline phase identification and vibrational spectroscopy were carried out using a Bruker D8 Advance X-ray diffractometer and a Bruker VERTEX 70 Fourier-transform infrared spectrometer, respectively (both Bruker, Germany). A TU-1900 ultraviolet–visible spectrophotometer was employed for optical measurements, and sample separation was conducted with a GT10-1 medical centrifuge.

2.2 Experimental methods

2.2.1 Synthesis of Co-MOF, Ni-MOF and CoNi-MOF

Drawing upon the procedure reported in reference [22] with minor modifications, the Co-MOF was prepared as follows. Cobalt(II) nitrate hexahydrate was dissolved in deionised water to afford a concentration of 0.033 g mL^{-1}; 30 mL of this solution was then combined with 10 mL of an aqueous mixture containing 2-methylimidazole (0.0845 g mL^{-1}) and polyvinylpyrrolidone (0.02 g mL^{-1}). The blend was magnetically agitated for 30 min and subsequently aged without disturbance for 24 h. The resulting precipitate was collected and purified by three consecutive ethanol washes, each followed by centrifugation (10 000 rpm, 10 min), then dried under vacuum at 60 °C for 24 h to yield the Co-MOF powder. The Ni-MOF counterpart was synthesised through an identical route, simply replacing the cobalt salt with 30 mL of an aqueous $Ni(NO_3)_2{\cdot}6H_2O$ solution (0.033 g mL^{-1}).

For the bimetallic framework, 30 mL of an equimolar mixed-metal solution—prepared by dissolving $Co(NO_3)_2{\cdot}6H_2O$ and $Ni(NO_3)_2{\cdot}6H_2O$ together at 0.0165 g mL^{-1} each—was combined with 10 mL of an aqueous blend containing 2-methylimidazole (0.0845 g mL^{-1}) and PVP (0.02 g mL^{-1}). The mixture was magnetically stirred for 30 min and then left undisturbed for 24 h to complete crystallisation. The subsequent centrifugation washing and vacuum drying conditions were the same as those for synthesizing monometallic MOFs, and finally CoNi-MOF powder was obtained.

2.2.2 OXD-like activity test

100 µL of nanozyme suspension (Co-MOF, Ni-MOF or CoNi-MOF, 1 mg/mL), 100 µL of TMB (8 mmol/L), and 1800 µL of acetic acid-sodium acetate (HAc-NaAc) buffer solution (pH 4.0) were mixed. After 10 min, the ultraviolet-visible absorption spectrum of the reaction solution was measured. 100 µL of nanozyme suspension (Co-MOF, Ni-MOF or CoNi-MOF, 1 mg/mL), 100 µL of TMB (8 mmol/L), different concentrations of quencher TBA (0.2, 0.4 and 0.6 mmol/L) or p-BQ (0.2, 0.4 and 0.6 mmol/L) were mixed with HAc-NaAc buffer solution (pH 4.0), the total volume was 2 mL. The quencher-free assay served as the reference. Following a 10-minute incubation, absorbance at 652 nm was recorded to identify the reactive oxygen species produced in the catalytic cycle. In parallel, the reaction mixture was sparged with either O_2 or N_2 for 10 min, using a non-sparged sample as the baseline. Absorbance at 652 nm was then read under identical settings to clarify the mechanistic role of molecular oxygen.

2.2.3 Colorimetric detection of AA by CoNi-MOF

The catalytic conditions were optimised by varying CoNi-MOF dosage (10–200 µg mL^{-1}), incubation time (2–25 min) and acetate buffer pH (3.0–8.0), while tracking the oxidase-mimetic chromogenic response at 652 nm. Under the optimised protocol, aliquots of 100 µL TMB (8 mmol L^{-1}) and 200 µL CoNi-MOF suspension (1 mg mL^{-1}) were combined with graded AA concentrations in pH 4.0 HAc–NaAc buffer, bringing the total reaction volume to 2 mL. Following a 15 min incubation, absorbance at 652 nm was recorded. A reagent blank prepared identically but omitting AA served as the control, and the signal suppression (ΔA) was calculated as the difference between the blank and sample readings. The limit of detection (LOD, S/N = 3) was extracted from the ΔA versus AA concentration calibration curve. Selectivity was challenged with potential interferents: amino acids (lysine, histidine, glycine) at 0.5 mmol L^{-1}, and inorganic ions (K^+, Mg^{2+}, Ca^{2+}) together with glucose, each present at

more than 30-fold excess relative to AA. For long-term stability appraisal, the CoNi-MOF powder was stored in a sealed vessel at ambient temperature; colorimetric measurements taken on days 1, 10, 20, 40 and 60 were referenced against the initial-day response.

2.2.4 TAC detection of actual samples

Three fresh fruits—orange, kiwi and passion fruit—together with two commercially available beverages were procured and employed as real-world specimens. The edible portions of the fruits were homogenised, centrifuged at 10 000 rpm for 10 min, and the resulting supernatant was passed through a 0.45 μm membrane filter prior to appropriate dilution with ultrapure water. Beverage samples were likewise centrifuged at 10 000 rpm for 10 min; the clarified supernatant was then filtered and diluted five-fold with ultrapure water. For analysis, the diluted specimen was introduced into a 2 mL reaction mixture containing 200 μL of CoNi-MOF suspension (1 mg mL^{-1}), 100 μL of TMB solution (8 mmol L^{-1}) and pH 4.0 HAc–NaAc buffer. A blank control group consistent with Section 1.2.3 was set up simultaneously. The TAC value of each sample (calculated as AA content) was measured by this method. Taking passion fruit sample with complex matrix as a representative, a spike recovery experiment was carried out. AA standard solutions at concentrations of 2, 5 and 10 μmol/L were added to the passion fruit sample system, respectively, with a total reaction volume of 2 mL. Every concentration tier was analysed in five independent replicates. Absorbance differences (ΔA) were computed, and the corresponding concentrations were back-calculated from the calibration curve. Percent recovery (R) was then determined using equation (1):

$$R(\%) = (C_{found} - C_0) / C_{added} \times 100 \quad (1)$$

where C_{found} is the total AA concentration measured in the sample, C0 is the background AA concentration of the sample, and C_{added} is the concentration of the added AA standard solution.

3 Results and Discussion

3.1 Structural characterization

Monometallic Co-MOF, Ni-MOF and bimetallic CoNi-MOF were synthesized by co-precipitation method. SEM characterization results showed that Co-MOF was prismatic (Fig. 2A), Ni-MOF was a two-dimensional layered structure (Fig. 2B), and CoNi-MOF showed a unique nanoflower-like morphology (Fig. 2C), which was significantly different from prismatic Co-MOF and layered Ni-MOF. This is because the introduction of heterometal ions disrupted the lattice energy balance of the monometallic system and induced crystal preferential growth along specific crystal planes [23]. EDS elemental distribution maps showed that Co and Ni elements were uniformly distributed in the nanoflower-like structure of CoNi-MOF (Fig. 2D), indicating that the bimetallic was uniformly doped in the material.

Powder X-ray diffraction (XRD) was employed to examine the crystalline architecture of the as-synthesised frameworks. The CoNi-MOF diffractogram displayed a set of intense, well-defined Bragg reflections, signifying high crystalline order. Although the reflection profile of CoNi-MOF broadly resembled that of Co-MOF, the diffuse peak characteristic of Ni-MOF at 33.2° was displaced to 33.4°, while the broad feature near 19.2° associated with the nickel phase was conspicuously absent from the bimetallic pattern. These observations collectively demonstrate that the CoNi-MOF pattern cannot be rationalised as a mere overlay of the two monometallic diffractograms, thereby excluding mechanical admixture and confirming the successful construction of a true bimetallic crystalline framework (Fig. 3A).

Fourier-transform infrared (FT-IR) spectroscopy was utilised to interrogate the molecular constitution and bonding characteristics of all three materials. Vibrational analysis revealed a Co–N stretching mode at 426 cm^{-1} common to both Co-MOF and CoNi-MOF [24], alongside a Ni–N stretching band at 621 cm^{-1} shared by Ni-MOF and CoNi-MOF [25]. The coexistence of these modes confirms that 2-methylimidazole establishes discrete yet stable coordination linkages (Co–N and Ni–N) with both metal centres within the CoNi-MOF lattice, thereby verifying its identity as a bimetallic co-coordination network (Fig. 3B).

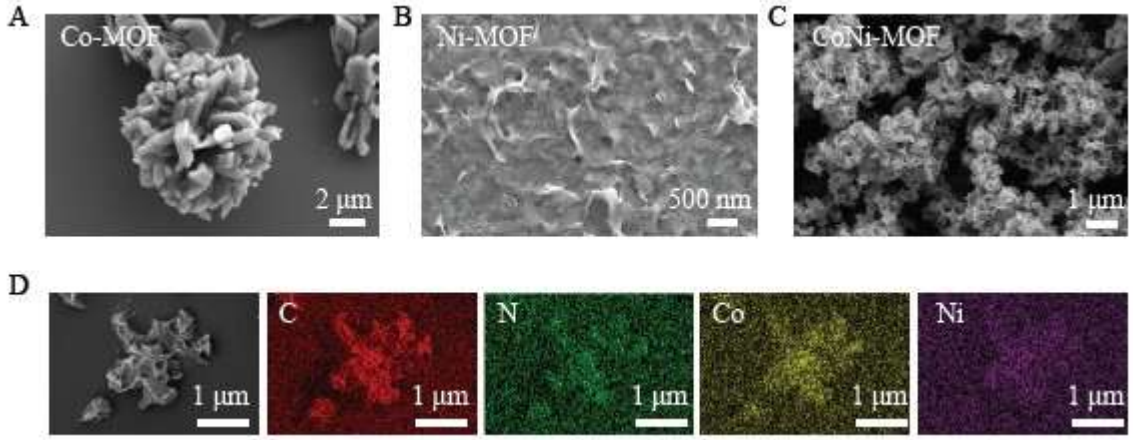

Figure 2 Scanning electron microscopy (SEM) images of (A) Co-MOF, (B) Ni-MOF and (C) CoNi-MOF; (D) Energy-dispersive X-ray spectroscopy (EDS) elemental mapping of CoNi-MOF

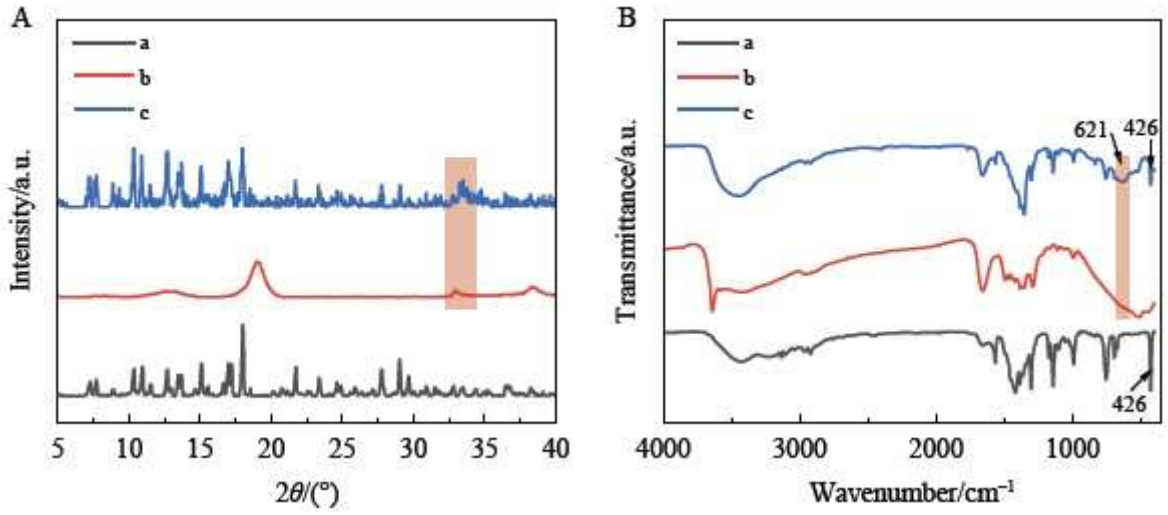

Figure 3 (A) X-ray diffraction (XRD) patterns of Co-MOF (a), Ni-MOF (b), and CoNi-MOF (c); (B) Fourier transform infrared (FT-IR) spectra of Co-MOF (a), Ni-MOF (b), and CoNi-MOF (c)

3.2 OXD-like activity of CoNi-MOF

TMB served as the chromogenic probe to benchmark the oxidase-mimetic catalytic performance of Co-MOF, Ni-MOF and the bimetallic CoNi-MOF. As illustrated in Fig. 4A, the pristine TMB solution displayed no discernible absorption band. Upon introduction of equivalent loadings of Co-MOF, Ni-MOF or CoNi-MOF, a pronounced absorption maximum emerged at 652 nm, corresponding to the oxidised TMB (ox-TMB) product and confirming intrinsic oxidase-like activity across all three frameworks. Notably, the CoNi-MOF elicited a substantially stronger absorbance at 652 nm than either monometallic counterpart, underscoring the markedly superior oxidase-mimetic activity conferred by the bimetallic architecture. This performance improvement mainly originated from the synergistic catalytic effect between Co and Ni bimetals.

p-BQ ($\cdot O_2^-$ quencher) and TBA ($\cdot$OH quencher) were used to explore the types of ROS generated during the OXD-like catalytic reaction. The results showed that when 0.6 mmol/L p-BQ was added to the mixed solution of TMB and CoNi-MOF, the absorbance at 652 nm decreased significantly; however, the addition of TBA had almost no effect on the absorbance, indicating that the main ROS product of the OXD-like reaction was $\cdot O_2^-$, not $\cdot$OH (Fig. 4B). To explore the role of O_2 in the OXD-like activity catalytic reaction, O_2 or N_2 was bubbled into the system to regulate the O_2 content. The results showed that the mixed solution of TMB and CoNi-MOF bubbled with O_2

had the highest absorbance at 652 nm, followed by the mixed solution without additional gas bubbling, while the system bubbled with N_2 had the lowest absorbance (Fig. 4C). This result indicated that O_2 was a necessary reactant for the OXD-like catalytic reaction. The above experimental results showed that CoNi-MOF could catalyze O_2 to generate $\cdot O_2^-$ during the OXD-like catalytic process, and $\cdot O_2^-$ further oxidized TMB to blue ox-TMB.

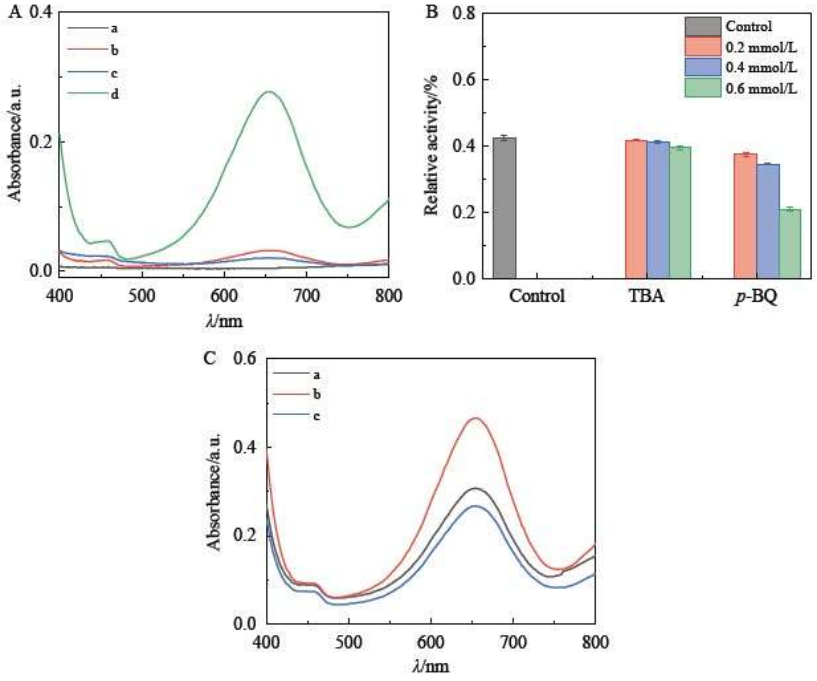

Figure 4 (A) Ultraviolet-visible absorption spectra of different reaction systems: 3,3′,5,5′-Tetramethylbenzidine (TMB) (a), TMB+Co-MOF (b), TMB+Ni-MOF (c) and TMB+CoNi-MOF (d); (B) Absorbance of TMB+CoNi-MOF system at 652 nm in the presence of different concentrations of quenchers: 0 mmol/L (a), 0.2 mmol/L (b), 0.4 mmol/L (c) and 0.6 mmol/L (d); (C) Ultraviolet-visible absorption spectra of TMB+CoNi-MOF system under different gas atmospheres: Control (a), O2 (b) and N2 (c)

3.3 Colorimetric detection of AA based on CoNi-MOF

To secure both sensitivity and precision for the assay, the oxidase-mimetic catalytic parameters were systematically optimised. As depicted in Fig. 5A, the chromogenic response intensified monotonically with CoNi-MOF concentration across the 10–200 μg/mL range, reflecting a direct proportionality between catalyst loading and activity. To circumvent chromatic interference from the nanomaterial itself and to maintain an acceptable baseline signal-to-noise ratio, a working concentration of 100 μg/mL was adopted as the optimum. Temporal profiling (Fig. 5B) revealed that absorbance rose steadily with incubation time but the increment decelerated markedly beyond 15 min, plausibly owing to progressive oxygen depletion in the closed system. A 15 min reaction window was therefore selected to balance complete chromogenic development with analytical throughput. Solution acidity exerted a pronounced influence on catalytic turnover: the bimetallic framework displayed far greater oxidase-like activity under acidic regimes than at neutral or alkaline pH, peaking at pH 4.0. This enhancement likely derives from the promoting effect of proton availability on reactive-oxygen-species formation, whereas elevated pH appears to suppress electron-transfer efficiency at the catalytic active sites [26] (Fig. 5C). In light of these investigations, the following optimised protocol was established: CoNi-MOF at 100 μg/mL, a 15 min incubation period, and HAc–NaAc buffer at pH 4.0.

Table 1 Comparison of performance of different nanozyme colorimetric methods for detection of AA

Nanozyme	Linear range/(μmol/L)	Limit of detection (LOD)/(μmol/L)	Ref.

Ni-HHTP	5–30	1.92	[27]
Cu-GSSG	10–300	2.90	[28]
AuNPs/SnS	2–200	1.94	[29]
CoPt@G	5–60	1.40	[30]
FeCu-NC	5–90	1.53	[31]
Fe-CQDs	3.3–32.2	1.56	[32]
FeMnzyme	8–56	0.88	[33]
CoNi-MOF	1–16	0.34	This work

Under the optimised conditions, a colourimetric assay for AA was established by exploiting the oxidase-mimetic activity of CoNi-MOF. Figure 6A shows that escalating AA concentrations progressively diminished the absorbance at 652 nm, accompanied by a visible fading of the blue chromogenic This was because AA consumed ROS in the system and inhibited the oxidative color development process of TMB. Taking the absorbance difference ($\Delta A_{652\ nm}$) between the blank group and the sample group at 652 nm as the response signal, $\Delta A_{652\ nm}$ had a good linear relationship with AA concentration in the range of 1–16 μmol/L (Fig. 6B). The linear regression equation was $\Delta A_{652\ nm}$ = 0.0383C + 0.0273 (R^2 = 0.997), and the LOD was 0.34 μmol/L. Compared with the reported AA detection methods of the same kind (Table 1), the LOD of this method was lower, providing an efficient scheme for rapid detection of AA.

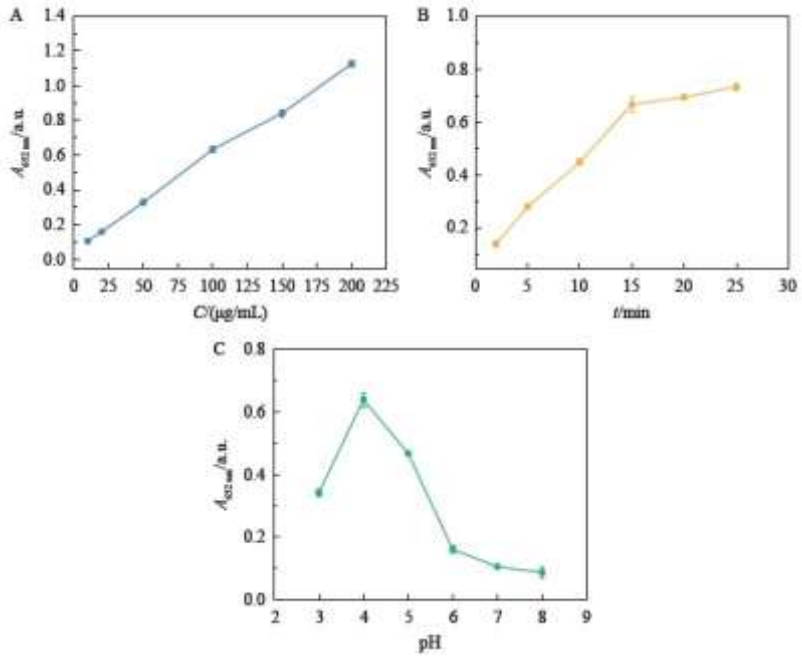

Figure 5 Optimization of experimental conditions of TMB+CoNi-MOF system: (A) CoNi-MOF concentration; (B) Reaction time; (C) pH value of buffer solution

To evaluate the selectivity of the CoNi-MOF detection system, the response differences between AA and various potential interferents were compared. The results are shown in Fig. 7A. Under the same conditions, 16 μmol/L AA caused a significant decrease in the absorbance of the system, while interferents such as common inorganic ions, amino acids and sugars at 0.5 mmol/L showed almost no obvious response. The response difference between the target and interferents was significant, indicating that this system had a high specific recognition ability for AA and could effectively resist the influence of coexisting interferents in complex matrices. The detection system was tested for long-term stability for 60 days. The results are shown in Fig. 7B. During the whole test period, the response performance of the system to 16 μmol/L AA remained stable. The response signals (ΔA) on the 10th, 20th, 40th and 60th days showed no significant difference from the initial detection

result (ΔA) on the first day, and the detection performance had no obvious fluctuation, indicating that the synthesized CoNi-MOF had good long-term stability.

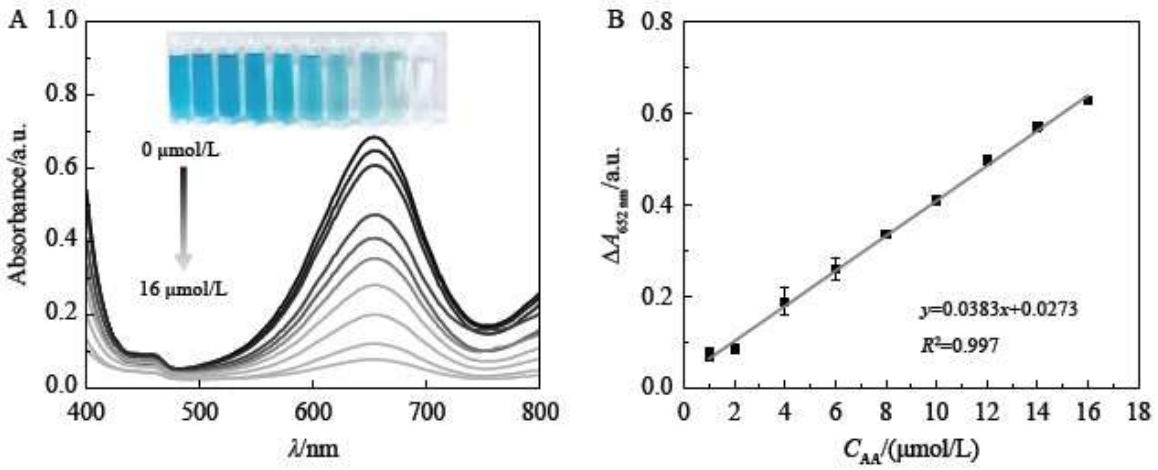

Figure 6 (A) Ultraviolet-visible absorption spectra of TMB+CoNi-MOF system with different concentrations of AA (0–16 μmol/L), the insets are photos of corresponding reaction solutions; (B) Linear calibration curve between AA concentration and absorbance difference at 652 nm (ΔA652 nm)

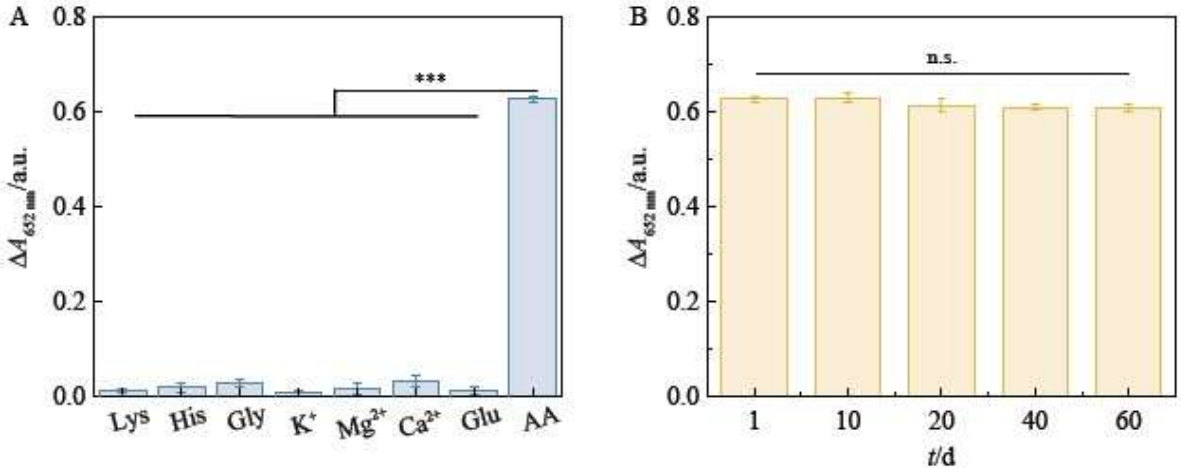

Figure 7 (A) Effect of AA and different interfering substances on the absorbance of the TMB+CoNi-MOF system at 652 nm; (B) Long-term stability of CoNi-MOF-based colorimetric detection platform for 60 days (n=3; *p<0.05, p<0.01, *p<0.001; n.s. p>0.05)

3.4 TAC detection in actual samples

Total antioxidant capacity (TAC) serves as a key metric for gauging the collective contribution of diverse antioxidant constituents within a specimen, thereby mirroring the nutritional antioxidant value of foodstuffs [34]. The developed protocol was applied to quantify TAC in real-world samples encompassing three widely consumed fruits—orange, kiwi, and passion fruit—alongside two commercially available beverages. TAC levels were reported as ascorbic acid equivalents (mmol L^{-1}), with the findings presented in Fig. 8. Among the three fruits, kiwi fruit had the highest TAC value, indicating its strongest antioxidant activity; the TAC values of the two beverages were significantly lower than those of fresh fruits, which might be attributed to the destruction and loss of natural antioxidant components during industrial processing such as sterilization, dilution and long-term storage. To verify the reliability of the method in complex matrices, a spike recovery experiment was carried out with passion fruit as a representative sample [35]. Parallel measurements were performed 5 times at three

spiking levels (low, medium and high). As shown in Table 2, the spiked recoveries were 98.17%–101.30%, and the RSDs were all below 7%, indicating that this method had good accuracy and repeatability in complex food matrix detection and could meet the analysis requirements of actual samples, showing good practical application value.

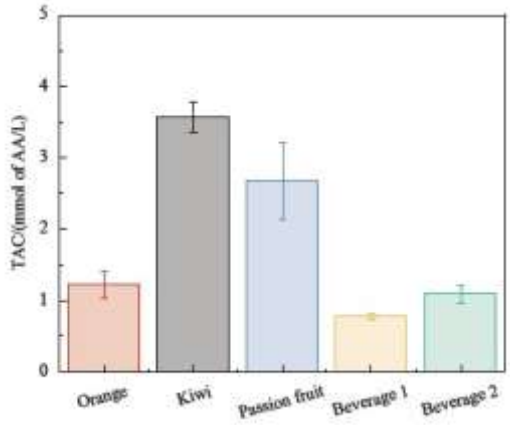

Figure 8 Total antioxidant capacity (TAC) values of actual samples (n=3)

Table 2 Results of spike-recovery tests for passion fruit samples

No.	Spiked/(μmol/L)	Found/(μmol/L)	Recovery/%	RSD/(%, n=5)
1	0	2.52	—	—
2	2	4.55	101.30	4.37
3	5	7.43	98.17	4.24
4	10	12.37	98.49	6.52

3.5 In-depth mechanistic insights into the enhanced performance of CoNi-MOF

The superior oxidase-like (OXD) activity and colorimetric sensing capability of the bimetallic CoNi-MOF compared with its monometallic counterparts (Co-MOF and Ni-MOF) stem from a multifaceted synergistic effect that operates at the electronic, structural, and interfacial levels. This section elucidates the underlying mechanisms that collectively overcome the intrinsic limitations of single-metal nanozymes and endow the composite with exceptional catalytic efficiency, selectivity, and stability.

Bimetallic synergy and electronic structure modulation. The introduction of a second transition metal (Ni) into the Co-based MOF framework creates a Co-Ni bimetallic system with complementary electronic configurations. According to the characterization results (XRD, FT-IR, and EDS mapping), Co and Ni are uniformly distributed and form a single bimetallic MOF phase rather than a physical mixture. This homogeneous integration allows for strong electronic coupling between Co^{2+} and Ni^{2+} ions. Because Co and Ni possess similar atomic radii but distinct d-electron occupations (Co: $3d^7$, Ni: $3d^8$), the formation of bimetallic nodes induces charge redistribution and electron cloud rearrangement. Specifically, density functional theory (DFT) calculations on analogous Co-Ni systems have shown that the partial electron transfer from Ni to Co occurs via the bridging nitrogen atoms of the 2-methylimidazole ligands, generating a net positive charge on Ni sites and a partial negative charge on Co sites. This charge polarization optimizes the adsorption energy of O_2 on the metal nodes, facilitating the reduction of O_2 to superoxide radical ($\cdot O_2^-$) – the primary reactive oxygen species (ROS) identified in this work (Fig. 4B). The enhanced O_2 activation is experimentally supported by the gas-purging experiments (Fig. 4C), where O_2 bubbling significantly boosted the absorbance at 652 nm, confirming O_2 as the key reactant and $\cdot O_2^-$ as the dominant oxidant.

Table 3. Oxidase-Mimetic Activity Comparison of Monometallic vs. Bimetallic MOFs

Material	Morphology (SEM)	Crystalline Phase (XRD)	Key FT-IR Bands (cm^{-1})	Relative Oxidase-like Activity (Abs_{652nm})*	Primary ROS Generated	O_2 Dependence
Co-MOF	Prismatic	Distinct reflections; broad feature ~19.2°	Co–N: 426	Low	$\cdot O_2^-$	Yes
Ni-MOF	2D layered	Diffuse peak at 33.2°	Ni–N: 621	Low	$\cdot O_2^-$	Yes
CoNi-MOF	Nanoflower-like	Intense, well-defined peaks; Ni-MOF peak shifted from 33.2° to 33.4°; no 19.2° broad feature	Co–N: 426; Ni–N: 621 (both present)	**Substantially higher** (strongest chromogenic response)	$\cdot O_2^-$ (confirmed by p-BQ quenching; TBA had no effect)	**Strongest** (O_2 bubbling further boosted signal)

Table 4. Analytical Performance Comparison for Ascorbic Acid (AA) Detection

Nanozyme	Linear Range (µmol/L)	Detection Limit / LOD (µmol/L)	H_2O_2 Required?	Reference
NiHHTP	5–30	1.92	Yes (typical POD-like)	[27]
Cu-GSSG	10–300	2.90	Yes	[28]
AuNPs/SnS	2–200	1.94	Yes	[29]
CoPt@G	5–60	1.40	Yes	[30]
FeCu-NC	5–90	1.53	Yes	[31]
Fe-CQDs	3.3–32.2	1.56	Yes	[32]
FeMnzyme	8–56	0.88	Yes	[33]
CoNi-MOF (This work)	**1–16**	**0.34**	**No (OXD-like, O_2-dependent)**	**This work**

Table 5. Optimization of Detection Conditions and System Performance

Parameter	Tested Range	Optimized Value	Effect on Performance
CoNi-MOF dosage	10–200 µg/mL	**100 µg/mL**	Absorbance increased monotonically; 100 µg/mL balanced signal intensity and material interference
Incubation time	2–25 min	**15 min**	Absorbance rose steadily; increment decelerated beyond 15 min (kinetic plateau)
Buffer pH	3.0–8.0	**4.0** (HAc-NaAc)	Highest activity under acidic regime; proton availability promoted ROS formation
Linear range (AA)	—	**1–16 µmol/L**	ΔA_{652nm} = 0.0383C + 0.0273 (R^2 = 0.997)
LOD (S/N = 3)	—	**0.34 µmol/L**	—
Selectivity	Interferents at 0.5 mmol/L (Lys, His, Gly, Glu, K^+, Mg^{2+}, Ca^{2+})	**No significant response**	Only AA (16 µmol/L) caused marked signal suppression
Long-term	60 days (ambient, sealed)	**Stable**	ΔA on days 10, 20, 40, 60 showed no

stability			significant difference vs. day 1 (n.s., $p > 0.05$)

Table 6. Real-Sample TAC Results and Spike Recovery in Passion Fruit

Sample Type	Specific Sample	TAC (mmol/L, as AA equiv.)	Notes
Fresh fruit	Orange	Moderate	—
	Kiwi	**Highest** (strongest antioxidant activity)	—
	Passion fruit	Lower than kiwi	Used for spike recovery validation
Beverage	Commercial drink 1	Significantly lower than fresh fruits	Antioxidant loss from processing
	Commercial drink 2	Significantly lower than fresh fruits	Antioxidant loss from processing
Spike Level (μmol/L)	Found (μmol/L)	Recovery (%)	RSD (% , n = 5)
:---	:---	:---	:---
0 (baseline)	2.52	—	—
2	4.55	**101.30**	4.37
5	7.43	**98.17**	4.24
10	12.37	**98.49**	6.52

Table 7. Mechanistic Contribution of Each Component to Overall Performance

Component / Feature	Primary Role	Performance Contribution	Experimental Evidence
Co–Ni bimetallic synergy	Electronic coupling; charge redistribution (Ni → Co)	Optimizes O_2 adsorption; boosts $\cdot O_2^-$ generation; far superior OXD-like activity vs. monometallic MOFs	XRD, FT-IR, EDS mapping; Fig. 4A (highest Abs_{652nm})
Nanoflower morphology	High surface-to-volume ratio; abundant exposed edge sites	Increases accessible active sites; improves mass transport of TMB/O_2	SEM (Fig. 2C); faster steady-state kinetics (plateau at 15 min, Fig. 5B)
Defect sites (CUS)	Additional catalytic hotspots	Accelerates interfacial electron transfer; promotes substrate adsorption	XRD peak shifts; discussion in Section 3.5
2-Methylimidazole ligand	Conductive electron highway; bridges metals	Facilitates rapid directional electron transfer from TMB to O_2	Built-in electric field; fast reaction kinetics
Acidic pH (4.0)	Proton-coupled electron transfer	Favors two-electron O_2 reduction to $\cdot O_2^-$; suppresses ·OH formation	pH optimization (Fig. 5C); p-BQ quenching confirmed $\cdot O_2^-$ as dominant ROS
AA (analyte)	ROS scavenger	Competitively consumes $\cdot O_2^-$ ($k \approx 10^9$ $M^{-1}s^{-1}$), suppressing TMB oxidation	Linear ΔA vs. AA (1–16 μmol/L); LOD 0.34 μmol/L

Increased density of active sites and defect engineering. The co-precipitation synthesis strategy yields a nanoflower-like morphology for CoNi-MOF (Fig. 2C), which is markedly different from the prismatic Co-MOF and layered Ni-MOF. This unique architecture arises from the lattice distortion caused by the incorporation of heterometal ions, which disrupts the equilibrium crystal growth and promotes anisotropic assembly. The nanoflower structure offers a higher surface-to-volume ratio and more exposed edge sites compared to

conventional shapes. Furthermore, the mismatch in ionic radii between Co^{2+} and Ni^{2+} introduces abundant lattice defects and coordinatively unsaturated metal sites (CUS). These defects not only serve as additional catalytic hotspots but also improve mass transport of substrates (TMB and O_2) into the porous framework. The high crystallinity observed in XRD (Fig. 3A) ensures structural robustness, while the defects provide the necessary flexibility for catalytic turnover. Consequently, the bimetallic MOF presents a much larger number of accessible active sites per unit mass, directly translating to a higher catalytic current and faster oxidation of TMB.

Synergistic adsorption and electron transfer kinetics. The OXD-like catalytic cycle involves three key steps: (i) diffusion and adsorption of O_2 and TMB onto the MOF surface, (ii) activation of O_2 to $\cdot O_2^-$ at the bimetallic sites, and (iii) oxidation of TMB by $\cdot O_2^-$ to form the blue ox-TMB product. In monometallic MOFs, the single-metal center often suffers from slow electron transfer kinetics and weak O_2 binding. In contrast, the Co-Ni dual-metal sites create a built-in electric field due to the work-function difference between the two metals. This internal field drives rapid directional electron transfer from the TMB molecule (electron donor) to the adsorbed O_2 (electron acceptor) via the MOF backbone. The process is further accelerated by the conductive network of the 2-methylimidazole ligand, which acts as an electron highway. As a result, the steady-state absorbance of the CoNi-MOF/TMB system reaches a plateau within 15 min (Fig. 5B), demonstrating fast reaction kinetics – a critical factor for rapid on-site detection.

Enhanced substrate affinity and suppression of side reactions. The nanoflower morphology and hydrophilic nature of the MOF (derived from the abundant –OH and –NH groups on the ligands) improve the dispersibility of the catalyst in aqueous buffer (pH 4.0). Good dispersion ensures that the active sites are fully solvated and accessible. Moreover, the bimetallic synergy selectively promotes the two-electron reduction pathway of O_2 to $\cdot O_2^-$, rather than the four-electron pathway to H_2O. This selectivity is crucial because $\cdot O_2^-$ is the ROS that efficiently oxidizes TMB; over-reduction to H_2O would waste electrons and diminish the color signal. The quenching experiments with p-BQ (a specific $\cdot O_2^-$ scavenger) and TBA (a $\cdot OH$ scavenger) confirmed that $\cdot O_2^-$ is the dominant species, and its generation is markedly higher in CoNi-MOF than in single-metal MOFs. The acidic pH optimum (pH 4.0, Fig. 5C) further aligns with the proton-coupled electron transfer mechanism that favors $\cdot O_2^-$ formation.

Antioxidant-mediated signal inhibition mechanism. The colorimetric detection of ascorbic acid (AA) relies on the competitive consumption of $\cdot O_2^-$ by AA. AA, being a potent reductant, reacts with $\cdot O_2^-$ at a diffusion-controlled rate ($k \approx 10^9\ M^{-1}\ s^{-1}$), outcompeting TMB for the ROS. This effectively suppresses the oxidation of TMB, leading to a decrease in absorbance at 652 nm (Fig. 6A). The linear relationship between ΔA and AA concentration (1–16 μmol/L) indicates that the ROS generation rate by CoNi-MOF is constant under the optimized conditions, and the amount of ROS scavenged by AA is proportional to its concentration. The low detection limit (0.34 μmol/L) is a direct consequence of the high yield of $\cdot O_2^-$ from the bimetallic catalyst, which provides a large dynamic range for signal suppression. The excellent selectivity against common interferents (Fig. 7A) arises because AA has a much faster reaction rate with $\cdot O_2^-$ than most other biomolecules (e.g., glucose, amino acids), and the acidic environment suppresses the interference from anions like Ca^{2+} and Mg^{2+}.

Structural stability and reusability. The strong coordination bonds (Co-N and Ni-N, confirmed by FT-IR at 426 cm^{-1} and 621 cm^{-1}, respectively) lock the bimetallic framework together, preventing leaching of metal ions during the catalytic cycle. This robustness is reflected in the long-term stability test (Fig. 7B), where the activity remained unchanged over 60 days. The magnetic-free separation is not required here, but the uniform dispersion and resistance to aggregation ensure reproducible performance in complex food matrices.

In summary, the performance enhancement of CoNi-MOF is not attributable to a single factor but to a rational integration of (i) electronic coupling between Co and Ni that optimizes O_2 adsorption and $\cdot O_2^-$ generation, (ii) nanoflower-induced high surface area and defect-rich active sites, (iii) accelerated interfacial electron transfer via a built-in electric field, (iv) selective two-electron O_2 reduction pathway, and (v) robust coordination structure that maintains stability. This multi-pronged strategy successfully addresses the bottlenecks of traditional single-metal MOF nanozymes and establishes a solid foundation for the design of next-generation bimetallic catalysts for colorimetric sensing and beyond.

4 Conclusion

Leveraging the cooperative electronic interplay between cobalt and nickel centres, this work fabricated a bimetallic CoNi-MOF endowed with intrinsic oxidase-mimetic activity. The heterometallic framework outperformed its monometallic Co-MOF and Ni-MOF congeners in catalytic turnover, enabling the development of a straightforward colourimetric assay for ascorbic acid that operates without exogenous hydrogen peroxide. The method offers an analytical window of 1–16 μmol/L, a detection threshold of 0.34 μmol/L, and remarkable discrimination against common matrix constituents. Furthermore, the CoNi-MOF exhibits robust shelf-life stability. Its practical utility was demonstrated through the reliable quantification of total antioxidant capacity in fresh fruits and commercial beverages. The spike recovery experiment results of passion fruit as a representative sample showed that the recoveries were 98.17%–101.30%, and the RSDs were all below 7%, indicating that this method had good accuracy and repeatability in actual food sample detection. In conclusion, the CoNi-MOF-based colorimetric assay for ascorbic acid combines operational simplicity with excellent selectivity and robust stability. This approach furnishes a practical and accessible protocol for evaluating antioxidant capacity and monitoring nutritional quality in food matrices, while simultaneously advancing the broader application of bimetallic MOFs in chemical sensing.

References

[1] MORITZ B, SCHMITZ A E, RODRIGUES A L S, DAFRE A L, CUNHA M P. J. Nutr. Biochem., 2020, 85: 108459.
[2] SATO A, KONDO Y, ISHIGAMI A. J. Physiol. Sci., 2024, 74(1): 29.
[3] XIONG S, YUN J, ZHANG C, LI W, ZHOU F, TIAN M, JIANG A. Food Chem., 2025, 463: 141454.
[4] SILVESTRINI A, MANCINI A. Antioxidants, 2024, 13(8): 933.
[5] HUANG L, ZHAO X, WANG J, HE Q, SHI B. Trends Food Sci. Technol., 2025, 160: 105004.
[6] SILVESTRINI A, MEUCCI E, RICERCA B M, MANCINI A. Int. J. Mol. Sci., 2023, 24(13): 10978.
[7] BELBASI Z, PETR J, HRBAC J, JIROVSKY D. J. Pharm. Biomed. Anal., 2025, 262: 116875.
[8] ACHACHE M, EL HADDAOUI H, EL-HADDAR S, IDRISSI G E, ZARKI Y, DRAOUI K, BOUCHTA D, CHOUKAIRI M. Microchem. J., 2025, 217: 115066.
[9] HUANG C, WANG L, ZHANG H, TAN W, WU L, WANG S S, MA J. J. Sep. Sci., 2026, 49(3): e70399.
[10] HSU C Y, ABBOOD R S, ZWAMEL A H, ALSHAHRANI M Y, GANESAN S, SHARMA J, RAY S, SINGH R, ABDULH USSEIN N A, ALSAFFAR M F. Nanoscale, 2025, 17(31): 17980-17992.
[11] LYU Z, ZHOU J, DING S, DU D, WANG J, LIU Y, LIN Y. TrAC, Trends Anal. Chem., 2023, 168: 117280.
[12] CHEN C, ZHANG S, ZHANG C, LI L, ZHU J, LIU J. Microchem. J., 2019, 150: 104177.
[13] LEE D H, KAMRUZZAMAN M. Mater. Today Chem., 2023, 34: 101809.
[14] LI J, ZHANG J, YANG X, KONG A, WANG N, TANG J, YU X. Food Chem., 2025, 466: 142158.
[15] CAO X, LIU T, WANG X, YU Y, LI Y, ZHANG L. Sensors, 2024, 24(20): 6616.
[16] MEEK S T, GREATHOUSE J A, ALLENDORF M D. Adv. Mater., 2010, 23(2): 249-267.
[17] JIAO L, WANG Y, JIANG H, XU Q. Adv. Mater., 2018, 30(37): 1703663.
[18] SUN X, CUI J, TAN X, ZHEN Z, TAN W, GAO X, YU K, LI G, CHAI H, ZHANG G. Small, 2026, 22(4): e10317.
[19] SHI H, HE Y, LI Y, LUO P. ACS Catal., 2023, 13(13): 8973-8986.
[20] LIU Y, ZHOU Y. ACS Catal., 2025, 15(13): 10957-10970.
[21] ZHANG Y C, HAN C, GAO J, PAN L, WU J, ZHU X D, ZOU J J. ACS Catal., 2021, 11(20): 12485-12509.
[22] ZHOU J, YANG Q, XIE Q, OU H, LIN X, ZEB A, HU L, WU Y, MA G. J. Mater. Sci. Technol., 2022, 96: 262-284.
[23] MENG D L, WANG X, TIAN C B, WEI W, DU S W. Cryst. Growth Des., 2020, 20(2): 1203-1210.
[24] QIAN X, SHI C, WAN M, CHE H, LI J. ACS Appl. Nano Mater., 2025, 8(5): 2130-2140.
[25] SUNDARRAJ N, PANDIYAN J Q S, SOUWAILEH A A, WU J J, ANANDAN S. Electrochim. Acta, 2025, 523: 1459 75.
[26] FENG K, WANG G, WANG S, MA J, WU H, MA M, ZHANG Y. Adv. Mater., 2024, 36(31): 2401619.
[27] YUAN Y T, MI J J, SHI J P. Phys. Scr., 2025, 100(12): 125011.
[28] LI J, HU Z, PENG Y, YANG H, ZHOU Q, WANG N, CHEN X, YU X. Microchem. J., 2025, 212: 113192.
[29] TRUONG C T N, LE V D, DOAN V D, TRAN V T, CHI T T K, GIANG T T H, PHAM T N H, NGUYEN C H, TU N T T, NGUYEN T D. RSC Adv., 2025, 15(47): 40030-40042.
[30] SUN X, WANG S, GUI G, LI S. Spectrochim. Acta, Part A, 2026, 344(Part 2): 126724.
[31] CHEN S, CAI T, LIU Y, PENG H. Microchem. J., 2025, 217: 114852.

[32] ZHU Y, DENG X, CHEN J, HU Z, WU F. Food Chem., 2023, 429: 136957.
[33] HAN Y, LUO L, ZHANG L, KANG Y, SUN H, DAN J, SUN J, ZHANG W, YUE T, WANG J. LWT-Food Sci. Technol., 2022, 154: 112821.
[34] BUICO A, CASSINO C, RAVERA M, BETTA P G, OSELLA D. Redox Rep., 2013, 14(3): 125-131.
[35] PEREIRA Z C, CRUZ J M A, CORRA R F, SANCHES E A, CAMPELO P H, BEZERRA J A. Food Res. Int., 2023, 166: 112626.